

Semi-automatic watershed medical image segmentation methods for customized cancer radiation treatment planning simulation

Oyeon Kum¹, Hye Kyung Kim², Nelson Max³

¹Pohang University of Science and Technology, Pohang, Korea

²Catholic University of Daegu, Daegu, Korea

³University of California, Davis, CA, USA

Abstract A cancer radiation treatment planning simulation requires image segmentation to define the gross tumor volume, clinical target volume, and planning target volume. Manual segmentation, which is usual in clinical settings, depends on the operator's experience and may, in addition, change for every trial by the same operator. To overcome this difficulty, we developed semi-automatic watershed medical image segmentation tools using both the top-down watershed algorithm in the insight segmentation and registration toolkit (ITK) and Vincent-Soille's bottom-up watershed algorithm with region merging. We applied our algorithms to segment two- and three-dimensional head phantom CT data and to find pixel (or voxel) numbers for each segmented area, which are needed for radiation treatment optimization. A semi-automatic method is useful to avoid errors incurred by both human and machine sources, and provide clear and visible information for pedagogical purpose.

Keywords Medical image segmentation · Watershed algorithm · Radiation treatment planning · CT data · Morphological mathematics

1. Introduction

Medical image segmentation is the process of clustering pixels in a medical image dataset to label them as anatomical structures with corresponding physiological properties. The labels resulting from this process have a wide variety of applications in medical research and visualization. Customized cancer radiation treatment planning [1] is a medical application where segmentation is beneficial. To optimize the cancer radiation treatment planning, we need to define the gross tumor volume, clinical target volume, and planning target volume in the anatomical areas of the patient's body, which may be characterized by the segmentation process. The distributions of pixel or voxel measurements of the patient's image data are treated as statistical samplings of the human anatomy and recognized using statistical pattern recognition.

The purpose of this study is to develop a pedagogically useful segmentation tool for medical images. Automation of digital image segmentation can be performed accurately, reproducibly, and efficiently using computers [2]. The best balance between full automation with computers and user interaction in a medical image segmentation method has been debated. Although many methods have moved on to full automation in medical image segmentation, the user interaction part is still required in one way or the other. In particular, semi-automatic method can be useful to avoid errors incurred by both human and machine sources, and provide clear and visible information for pedagogical purpose.

2. Materials and methods

The watershed algorithm classifies pixels into regions using mathematical morphology [2]. There are two different commonly used watershed algorithms: bottom-up and top-down. A bottom-up algorithm first finds basins and then the watersheds are the

voxels not in any basin. A top-down algorithm first computes a complete partition of the image into basins and subsequently finds watersheds by boundary detection. This assumes a multi-scale differentiable operator and consequently floating point operations. We used both methods in this study. The drawback of watershed segmentation is that it produces a region for each local minimum, resulting in oversegmentation. To alleviate this problem, a graph merging algorithm is used with a threshold value of the watershed depth. Thus, this technique is very flexible in that it does not produce a single image segmentation but rather a hierarchy of segmentations from which a single region or set of regions can be extracted a priori using a threshold, or interactively, with the help of a graphical user interface.

In this study, we have made efforts to develop interactive semi-automatic medical image segmentation algorithms with a graphical user interface for applications such as cancer radiation treatment planning. We developed three codes for medical image segmentation; the CT reader, the in-house hybrid merging watershed segmentation code, and another segmentation code using the free library in the insight segmentation and registration toolkit (ITK) [3]. The CT reader reads a DICOM format dataset to make a file containing Hounsfield values in a structured ASCII format, which is used as an input data file for the in-house and ITK library codes. An additional hybrid merging algorithm with a threshold overcomes oversegmentation of the image due to the high sensitivity to gray scale image variation.

The ITK library code also reads the structured input data and produces a segmented output image and a corresponding ASCII format file showing segmented regions with different levels. Because this code uses many parameters for adjusting the size of segmentation, such as conductance, iteration number, threshold, level, and principle component, we need to find the best parameter values for a given section of the CT data. By running the two programs interactively, we can find the best-fit parameters to extract anatomical sections of the human body semi-automatically. The graphical user interface was implemented based on the visualization toolkit (VTK).

3. Results and discussion

The aim of this work is to confirm the feasibility of image segmentation to divide pixels into regions for calculations of the optimization matrix in radiotherapy treatment planning and to differentiate different organs to define the gross tumor volume, clinical target volume, and planning target volume in the anatomical areas of the patient's body semi-automatically.

We applied our algorithms to segment two- and three-dimensional head phantom CT data. Figure 1 shows two-dimensional segmentation results. The original CT slice is on the upper left-hand side. The threshold value is given as the percentage of the maximum depth. As the threshold value (T) increases, the number of segments (S) decreases. This property is very useful for selecting a focused anatomical region automatically. All the pixels (or voxels) in the focused anatomical region have the same labels to represent this region. A graph merging algorithm is used to adjust the number of labelled regions. The computing time for two-dimensional problem is a few second using a personal computer.

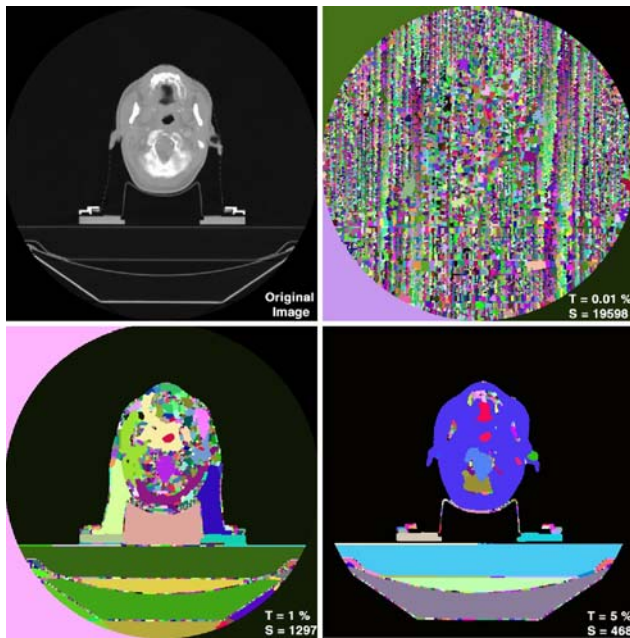


Fig. 1 Two-dimensional image segmentation using watershed algorithms. The original head phantom CT slice is on the upper left-hand side. The threshold value is given as the percentage of the maximum depth. As the threshold value (T) increases, the number of segments (S) decreases

During radiation therapy, the irradiating beams pass through a patient, killing both carcinoma and normal tissues [4]. Thus, the radiation treatment must be carefully planned to deliver a clinically prescribed dose to the target volumes containing carcinoma cells, while neighboring organs at risk and normal cells are spared. To optimize the beams, we need to extract pixel coordinate for each group of organs. The ASCII format output file is very useful to find the exact pixel coordinates for a region of interest.

Figure 2 shows three-dimensional semi-automatic region extraction and registration procedures from the head phantom

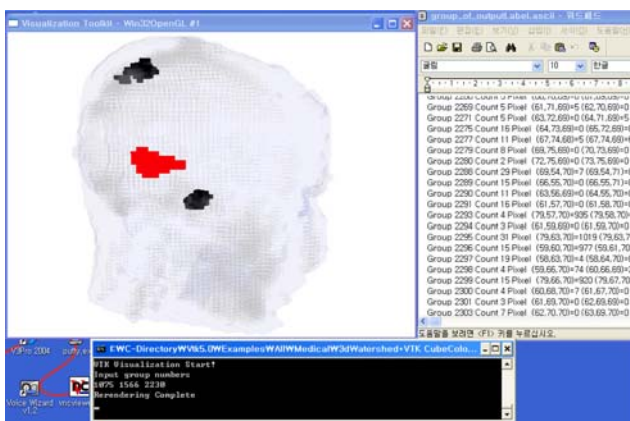


Fig. 2 Three-dimensional semi-automatic region extraction and registration procedure. The upper left-hand side window shows a transparent head phantom and three chosen regions. The upper right-hand side ASCII file includes all information about segmentation, number of total segmented volumes, number of pixels for each segmented volume, and Hounsfield value for each pixel

CT data. The figure shows three windows, the three-dimensional transparent image output window, the ASCII file output window including group information and the Hounsfield values for pixels, and the command input window. A semi-automatic procedure is very convenient at this stage because we can add or remove a group of regions semi-automatically with the help of the graphical user interface if the volume is not exactly matched.

From the command input window, we can add, replace, and remove any region. The results are shown as coloured boxes in the three-dimensional transparent image output window. The detailed voxel information is included in the ASCII format output file which is used for constructing an optimization matrix. Thus, the main advantage of both watershed algorithms is that it directly gives a hierarchical segmentation in which all the boundaries are evaluated separately for each local minimum, allowing one to choose the desired level of regions after segmentation process as shown in Fig. 2.

4. Conclusions

We developed four computer codes (two watershed segmentation codes, a CT data management code, and a scientific data visualization code) for medical image segmentation and registration for radiotherapy planning. We applied our algorithms to analyze head phantom CT data and could semi-automatically find pixel addresses of the interesting anatomical regions for the use of treatment optimization simulations. Our codes can be used to extract and register the organs in the CT image data semi-automatically using a graphical user interface. We found that the semi-automatic method was useful to avoid errors incurred by both human and machine sources, and provided clear and visible information for pedagogical purpose. Further activity in upgrading of the codes includes better rendering algorithms to recognize anatomical structure of organs in three-dimensional CT data.

References

1. Kum O (2007) Telematics-based on-line client-server/client collaborative environment for radiotherapy planning simulations. *Med Bio Eng Comput* (submitted)
2. Roerdink J, Meijster A (2001) The watershed transform: definition, algorithms and parallelization strategies. *Fund Inform* 41:187–228
3. Yoo TS (ed) (2004) *Insight into images*. A K Peters: Wellesley, Massachusetts
4. Kim HK, Kum O (2006) Development of a parallel electron and photon transport (PMCEPT) code II: absorbed dose computation in homogeneous and heterogeneous media. *J Korean Phys Soc* 49(4):1640–1651

3D segmentation of liver, kidneys and spleen from CT images

György Bekes¹, László G. Nyúl², Eörs Máté², Attila Kuba², Márta Fidrich¹

¹GE Hungary ZRt. Healthcare Division, Hungary

²Department of Image Processing and Computer Graphics, University of Szeged, Szeged, Hungary

Abstract The clinicians often need to segment the abdominal organs for radiotherapy planning. Manual segmentation of these organs is very time-consuming, therefore automated methods are desired. We developed a semi-automatic segmentation method to outline liver, spleen and kidneys. It works on CT images without contrast intake that are acquired with a routine clinical protocol. From an initial surface around a user defined seed point, the segmentation of the organ is obtained by an active surface algorithm. Pre- and post-processing steps are used to adapt the general method for specific organs. The evaluation results show

that the accuracy of our method is about 90%, which can be further improved with little manual editing, and that the precision is slightly higher than that of manual contouring. Our method is accurate, precise and fast enough to use in the clinical practice.

Keywords Radiotherapy · Computer assisted image analysis · Image segmentation

1. Introduction

In radiotherapy (RT) planning, clinicians (radiologist, dosimetrists) must determine the outline of a few critical structures on a large number of 2D images. Manually drawing the individual contours on a contiguous set of 2D slices is very time consuming. Using automated image segmentation could save tremendous time and effort, and increase precision by eliminating subjectivity of the clinician.

There are several published methods about segmentation of CT images. Most of them are some variants of the region growing, active surface, or threshold-classification algorithms. In addition, the methods are often based on some statistical, anatomical, or geometrical model. There are a few algorithms developed specially to liver, spleen or kidney segmentation. The region-growing algorithm [1] automatically learns its homogeneity criterion from characteristics of the region to be segmented. The method presented in [2] aims at automatically extracting the liver structure from abdominal CT scans using a priori information about liver morphology and standard digital image-processing techniques like graylevel thresholding, Gaussian smoothing and eight-point connectivity tracking. Another approach is to apply m-rep model [3] for finding boundaries of multidimensional objects in scenes. The method described in [4] aims at utilizing atlas-based segmentation, wherein first the atlas-based contour is matched (using landmark point pairs) to patient's slices. This gives the initial contour to the active contour method. The kidney-specific algorithm presented in [5] uses an active surface approach combined with a kidney shape model. The shape of the kidney is given by non-uniform rational B-splines and defined by a priori statistical information.

2. Method

First we describe the theoretical background of our method, then we show how to use it for segmentation of the target organs.

2.1. Active surface

The active surface *minimizes an energy function* incorporating several properties of the image and the surface. The *iterative process* starts from the initial surface, and then at each iteration step, various forces are applied to move the surface vertices until all vertices stop moving or a predefined number of iteration is reached. The output is a closed surface given by a triangular mesh representing the organ. The energy function is the sum of the internal spline energy (E_{int}), a measure of the attraction of image feature (E_{im}) and the external constraint (E_{constr}).

The surface is discretized at the beginning and a discrete optimization problem is solved. Instead of energy minimization, we apply discrete forces on each boundary point and determine the equilibrium of these forces using a gradient method. The following forces are applied to move the vertices. *Image force* is represented by the normalized gradient of the image energy. *Local move force* is used to move the vertices with one unit in the direction of the resultant vector of the normals of the neighboring faces (that approximates the surface normal at the vertex) and it corresponds to the external constraint. If the vertex is located in "probable object region", local move becomes inflation; while in the opposite case, local move becomes deflation. *Smoothing force* corresponds to the internal energy and is intended to keep the shape smooth moving the point toward the center of gravity of its neighboring points.

As the surface expands or shrinks, more or fewer points/edges/faces are needed to represent the smooth surface. Even when using the smoothing force, it is occasionally necessary to adjust the number of distribution of nodes in the representation and, therefore, re-triangulation of the surface is desired. One approach to the *refinement of a triangular mesh* is to split triangles if their edges become too long, or merge vertices that get too close. This approach can be used to keep the surface model compact, uniform and topologically correct, but it cannot *handle topological changes*. We chose the topology adaptive surfaces or T-surfaces [6], which exploit an affine cell image decomposition (ACID) framework. ACID enables active contours and surfaces to grow into complex structures and even to change topology as necessary. During the iteration, after a certain number of deformation steps, the surface needs to be re-parameterized in order to maintain its compact and efficient representation. A novel way of surface re-parameterization is described below.

The ACID grid is applied, intersections are determined between the surface elements and the grid and a new surface is created by using the intersection points as new vertices. We found in our 3D experiments, that the original method and its working conditions do not always provide correct results. The original approach assumes that only "valid" combinations of intersection points may occur on the edges of a grid cell. However, "invalid" configurations of intersection points also occurred in our trials (1, 2, 5, 6 intersection points on the edges of a single tetrahedron, or special combinations of 3 or 4 intersection points). The original algorithm (described for 2D) used a region-growing-like algorithm to fill the volume that has been included by the deformed surface and was not "inside" the object previously. Due to the anomalies along the surface, the filling algorithm leaked out.

In order to solve these problems we *extended the ACID with a new scan-line algorithm*. Scan-lines are cast according to the ACID grid, and intersections between the scan-lines and the surface elements are computed and stored. Each intersection point is also labeled (INSIDE/OUTSIDE) indicating the orientation of the surface element at that point, that is, the cast line may hit the surface element from the inside of the object or from the outside. If for some reason the scan-lines do not agree on labeling a grid point, corrections are made to the grid and scan-line data structure. This consolidation is achieved by dropping intersection points from scan-lines if they turn out to disagree with the labeling, or new points may be inserted at certain places for similar reasons. At the end, there are either zero, three or four intersection points of well defined configurations on the edges of each grid cell.

2.2. Segmentation

The general active surface method is extended with pre- and post-processing steps to solve particular problems characteristic to the target organs (liver, spleen, and kidney). These additional functions incorporate anatomical knowledge. The method consists of the following steps.

Pre-processing applied on the input CT images:

- A special edge-preserving filter is used to reduce image noise.
- Detect the ribs in each axial and coronal slice of the volume and draw straight lines between them. This will constrain the active surface and is necessary, because the model often moves into muscles between the ribs due to their similar intensities with the liver and the spleen. Create initial surface:
- Initial surface is created around the user given seed points or curve. In case of liver and spleen, an initial curve should be drawn in the middle of the organ. In case of the kidneys, the segmentation is started from two seed points specified at the top and bottom end of the organ.

- In case of the kidneys, a model is created on the fly using the two seed points, and a special model force is generated. Deformation:
- The surface is deformed and regularly re-parameterized until a predefined number of iteration is reached. Post-processing:
- Apply 2D active contour to segment the left lobe of the liver more accurately.
- Smooth the resulting surface.

3. Result

By radiologists on 40 abdominal CT examinations to check the usability of the method. The set was randomly selected from a database of images acquired for various purposes at different institutions with different models of GE manufactured CT scanners (Fig. 1).

Three sets of measures were used: accuracy, precision, and efficiency (see Table 1).

True positive (TPVF), false positive (FPVF) and false negative (FNVF) volume fractions measure the *accuracy* of the method by comparing the segmented result with a “gold standard” that was created from manual segmentations of three radiologists. The error arises mostly from false negatives, i.e., parts of the liver, missed by the method but included by the physicians in manual outlining. These usually include the portal region and the thin lobes of the liver. In case of the kidneys, incorrect seed point selection was causing problems. We found that a short practice can considerably improve the correctness of the user-given seed points.

The intra-operator repeatability (wherein the same segmentation task was performed three times by the same user) and inter-operator reproducibility (wherein three users performed the same segmentation tasks) show the *precision* of the method. These tests were executed for manual drawing as well. The comparison indicates that the automated method has slightly higher precision than the manual.

The clinicians were also asked to fill out a *questionnaire* to provide information about possible problems and special needs. This questionnaire confirmed the usability of the result in clinical practice and the occasional need for small manual corrections. The *efficiency* of the method was measured on a HP workstation xw8200 with 2 GB memory and Intel Xeon 3400 processor.

4. Discussion

We created a new, generally usable active surface method that is solved as a discrete problem, where the deformation is performed by forces and the topological changes are handled by a scan-line



Fig. 1 Results of the organ-specific active surface method

Table 1 Statistics of the clinical evaluation: accuracy, precision and efficiency

Organ	Accuracy (%)			Precision (%)		Running time (s)
	TPVF	FPVF	FNVF	Inter-op.	Intra-op.	
Liver	83.57	5.37	16.43	94.06	94.67	22.4
Right kidney	91.19	17.10	8.81	91.33	94.64	9.2
Left kidney	87.66	15.95	12.34	91.84	92.61	9.05
Spleen	86.39	11.88	13.61	94.83	93.71	14.7

based algorithm. Pre- and post-processing steps are used to adapt the general method for organ specific problems, and to improve the accuracy.

The results show that our method is sufficiently fast and effective for use in clinical practice. The method is integrated into the Advantage Sim product of GE Healthcare and is used at several clinical sites. There are, however, some key points where the method can be further improved (e.g. better detection of thin left lobes of the liver). The clinicians also expressed their need for an intuitive 3D editing tool.

References

1. Pohle R, Toennies KD (2001) A new approach for model-based adaptive region growing in medical image analysis. In: Proceedings of the 9th of CAIP: pp 238–246
2. Bae KT, Giger ML, Chen CT, Kahn CE (1993) Automatic segmentation of liver structure in CT images. *Med Phys* 20:71–78
3. Pizer SM, Fritsch DS, Yu L, Johnson VE, McAuliffe M, Chaney EL (1997) A probabilistic approach using deformable organ models for automatic definition of normal anatomical structures for 3D treatment planning. In: Proceedings of the 38th ASTRO Meeting.
4. Qataneh SM, Noz ME, Hyodymaa S, Maguire GQ Jr, Kramer EL, Crafoord J (2003) Evaluation of a segmentation procedure to delineate organs for use in construction of a radiation therapy planning atlas. *Int J Med Inform* 69(1):39–55
5. Tsagaan B, Shimizu A, Kobatake H, Miyakawa K (2002) An automated segmentation method of kidney using statistical information. In: Proceedings of the 5th MICCAI, pp 556–563
6. McInerney T, Terzopoulos D (1999) Topology adaptive deformable surfaces for medical image volume segmentation. *IEEE Trans Med Imag* 18(10):840–850

Deformable 4DCT lung registration with vessel bifurcations

A. Hilsmann^a, T. Vik^a, M. Kaus^a, K. Franks^b, J.-P. Bissonette^b, T. Purdie^b, A. Beziak^b, T. Aach^c

^aPhilips Research Europe, Hamburg, Germany

^bPrincess Margaret Hosp., Toronto, Canada

^cRWTH Aachen University, Aachen, Germany

Abstract In radiotherapy planning of lung cancer, breathing motion causes uncertainty in the determination of the target volume. Image registration makes it possible to get information about the deformation of the lung and the tumor movement in the respiratory cycle from a few images. A dedicated, automatic, landmark-based technique was developed that finds corresponding vessel bifurcations. Hereby, we developed criteria to characterize *pronounced* bifurcations for which correspondence finding was more stable and accurate. The bifurcations were extracted from automatically segmented vessel trees in maximum inhale and maximum exhale CT thorax data sets. To find corresponding bifurcations in both data sets we used the shape context approach of Belongie et al. Finally, a volumetric lung deformation was obtained using thin-plate spline interpolation and affine registration. The method is evaluated on 10 4D-CT data sets of patients with lung cancer.

Keywords Medical image processing · Landmark-based elastic registration · Lung registration · Radiotherapy planning

1. Introduction

In radiotherapy planning one important aspect is to determine the target volume that is to be treated with radiation. Physiological movement of patient or organs, e.g. breathing motion, affects the definition of the target volume. In the context of lung tumor radiation planning respiratory models and the movement of

tumors over the respiratory cycle are currently being investigated. Deformable image registration has the potential to reduce geometric uncertainty, and provides the opportunity to increase treatment accuracy and precision by optimizing treatment in response to anatomical changes. This may allow for dose escalation. In order to capture movements of the inner lung, landmark based registration with landmarks on the inner vessel tree of the lung seems to be most promising because the vessels fill out the entire lung. Automatic landmark localization is important for clinical applications, as manual selection is time-consuming and often inaccurate.

2. Methods

2.1. Landmark extraction

Landmarks were extracted from the inner vessel tree of the lung. For vessel tree segmentation we used a front propagation algorithm [1, 2] that outputs a centerline representation of the vessel tree. The algorithm was extended to determine seed points automatically on the vessels. From the centerline we selected *pronounced* vessel bifurcations as landmarks. These bifurcations are formally defined as follows:

- The bifurcation consists of three vessel branches with radii r_i , $i = 1, 2, 3$.
- $1/m \sum r_i > \bar{R} - \sigma_R$ where \bar{R} and σ_R denote the average and standard deviation of all radii in the centerlines of the whole vessel tree.
- $\forall r_i : |r_i - \text{median}(r_i)| / \text{MAD}(r_i) < 2$ where $\text{MAD}(r_i)$ is the median absolute deviation ($\text{MAD}(X) = \text{median} |x_i - \text{median}(X)|$ with a population $X = (x_1, x_2, \dots, x_n)$ of the radii of branches at that particular bifurcation. Thereby we account for differences in parts of the vessel tree from one breathing state to the other that may cause segmentation differences in both images. Correspondence finding from those bifurcations was more stable and accurate than correspondence finding with all bifurcations.

2.2. Landmark matching

In order to define point correspondences in the lung we matched the vessel trees using features extracted from bifurcations. The 2D shape context as a regional shape descriptor was first introduced by Belongie et al. [3]. A 3D modification has already been applied to tree-like structures like the bronchial tree or coronal arteries with good results [1]. The basic idea of the shape context is that a shape is represented by a set of n points sampled from the contours on the shape [3]. Each of these points is characterized by its local adjacencies given by the $n - 1$ vectors originating from it to all other sample points on the shape. These vectors express the entire shape distribution relative to the reference point. As the full set of vectors is too detailed the shape is described by a coarse histogram. For each landmark-bifurcation we compute a 3D spherical histogram [1] in which the number of the displacement vectors to all remaining centerline points are counted for each bin. This histogram forms the feature vector. Assume a set of points $C = (c_1, c_2, \dots, c_n)$, $c_i \in \mathbb{R}^3$, $i = 1, \dots, n$ being centerline points from the vessel tree and a set of points $P = (p_1, p_2, \dots, p_m) \subset C$, $m < n$, $p_i \in \mathbb{R}^3$ being selected bifurcations of the vessel tree. For each bifurcation p_j we capture the local shape represented by all centerline points c_i as seen from that bifurcation in the 3D shape context. The displacement vectors $d_i = p_j - c_i$, $d_i \in \mathbb{R}^3$ from the reference bifurcation p_j to the remaining centerline points c_i are expressed in spherical coordinates $d_i(r, \theta, \varphi)$ and the number of displacement vectors is counted for each bin. Hereby, the angles φ and θ are quantized linearly and the radius r is quantized logarithmically making the descriptor more sensitive to positions of nearby sample points than to those far away. This histogram is said to be the shape context of the point p . We normalize the histogram and additionally weight each bin with its volume, i.e. we record the density instead of the frequency.

Assuming we are given two point sets $P = (p_1, p_2, \dots, p_m)$, $p_i \in \mathbb{R}^3$, $i = 1, \dots, m$ and $Q = (q_1, q_2, \dots, q_n)$, $q_j \in \mathbb{R}^3$, $j = 1, \dots, m$ being bifurcations of the maximum inhale and maximum exhale vessel trees, the cost function that measures the cost of matching the points p_i and q_j is given by the χ^2 -distance:

$$d_{\chi^2}(p_i, q_j) = \frac{1}{2} \sum_{d=1}^D \frac{(h_{dp_i} - h_{dq_j})^2}{h_{dp_i} + h_{dq_j}} \quad (1)$$

Corresponding landmarks in the maximum inhale data set to the maximum exhale data set are determined by minimizing the cost function.

2.3. Transformation estimation

Having identified the corresponding landmarks we estimate a volumetric transformation u that maps the maximum exhale landmark set $\{p_i\}$ onto the maximum inhale landmark set $\{q_i\}$ ($u(p_i) = q_i$). The transformation can be

1. an affine transformation that is determined by an least squares approach minimizing the quadratic error between the actual and estimated positions or
2. an elastic transformation using thin-plate spline interpolation between the irregularly distributed bifurcations [4].

3. Results

3.1. Data

4D-CT data sets with voxel dimensions of $0.98 \times 0.98 \times 2.5$ mm (left-right/LR, anterior-posterior/AP, inferior-superior/IS) of ten patients with lung cancer were analyzed. Eighteen corresponding vessel bifurcations were manually determined by an experienced physician in both phases. These points are referred to as *ground truth* points in the following. The *ground truth* points were selected such that three points lie each in the regions left upper lung (LUL), left lingular (Lling), left lower lung (LLL), right upper lung (RUL), right middle lung (RML) and right lower lung (RLL).

3.2. Ground truth analysis

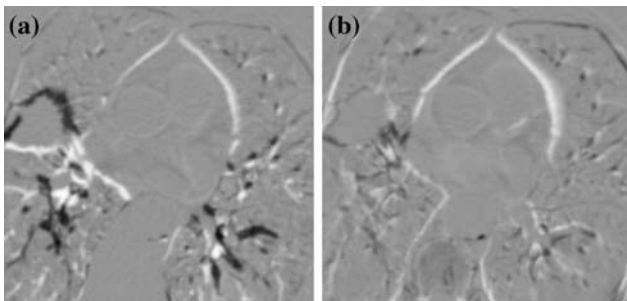
We applied the transformation estimated from the automatically extracted landmarks to the *ground truth* point set from the maximum exhale phase and its estimated positions in the maximum inhale phase were compared to the actual positions of the ground truth points. Ideally, the estimated position coincides with the actual position. The differences between these positions are referred to as *landmark discrepancies* in the following. The registration result is reported as $\bar{d}_{gt} \pm \sigma_{d_{gt}}$ where \bar{d}_{gt} denotes the average of all landmark discrepancies and $\sigma_{d_{gt}}$ is the standard deviation. The average absolute landmark discrepancies were reduced from 1.3 ± 1.13 mm to 1.06 ± 0.95 mm in LR-, from 1.76 ± 1.32 mm to 1.24 ± 1.27 mm in AP- and from 4.39 ± 5.03 mm to 1.86 ± 1.94 mm in IS-direction with thin-plate spline interpolation. The registration error using affine registration was 1.224 ± 1.69 mm (LR), 1.44 ± 2.02 mm (AP) and 2.30 ± 3.22 mm (IS). The average Euclidean distance between the *ground truth* points was 2.85 ± 2.11 mm for thin-plate spline interpolation and 3.40 ± 2.38 mm for affine registration. A paired *t*-test showed that the alignment accuracy was significant in all six regions of the lung referred to the breathing motion (see Table 1). A second paired *t*-test showed that in the upper and middle lung the thin-plate spline interpolation performance is significantly better than the performance of an affine registration (see Table 1). In the lower lung where the deformation is largest both transformations do not differ significantly.

3.3. Difference images

The second validation method relies on the difference images before and after registration. We transform the maximum inhale image on the maximum exhale image by applying the transformation

Table 1 Paired *t*-tests with 29 degrees of freedom

Regions	one-sided paired		two-sided paired	
	<i>t</i> -test align. accuracy – magn. of motion		<i>t</i> -test affine reg. – thin-plate splines	
	<i>t</i> -value	<i>P</i> -value	<i>t</i> -value	<i>P</i> -value
LUL	1.89	0.03500	2.13	0.02100
Lling	3.03	0.00260	2.08	0.02400
LLL	6.72	0.00005	0.18	0.43000
RUL	1.51	0.07100	3.53	0.00070
RML	3.31	0.00200	2.59	0.00740
RLL	6.75	0.00050	1.49	0.07403

**Fig. 1** Difference images in the axial plane before (a) and after (b) registration

estimated from the automatically extracted landmarks backwardly. We obtain a transformed version of the inhale image that, in the ideal case, is equal to the exhale image. Comparing the difference images before and after registration provides us with information about the registration result that depends on the image information only. Figure 1 presents an example of difference images in the axial and the sagittal plane. From the observation of the difference images it becomes obvious that the differences between the images are reduced near the vessels and the tumor and furthermore near the diaphragm.

4. Discussion and conclusion

In order to assess breathing motion information, a landmark-based registration technique with automatically extracted *pronounced* vessel bifurcations was developed. The average resulting registration error was 2.85 ± 2.11 mm for thin-plate spline and 3.40 ± 2.38 mm for affine registration. Referring to other landmark-based lung registration methods, Urschler et al. [5] used point correspondences from lung and diaphragm surfaces for a thin-plate spline registration and achieved mean registration errors in the range of 5–9 mm in experiments on CT sheep scans with voxel dimensions of $0.5 \text{ mm} \times 0.52 \text{ mm} \times 0.6 \text{ mm}$. Coselmon et al. [6] applied gray value based image registration using mutual information and thin-plate spline interpolation. They achieved an alignment accuracy of 1.7, 3.1 and 3.6 mm in the LR-, AP- and IS-directions. Compared to these registration results we obtain smaller registration errors despite lower image resolution. Visual inspection of the difference images showed that the method performs well near the vessels and the tumor as well as in regions near the diaphragm.

References

1. Bülow T, Lorenz C, Renisch S (2004) A general framework for tree segmentation and reconstruction from medical volume data. In: MICCAI 2004 (1), pp 533–540

2. Bülow T, Lorenz C, Wiemker R, Honko J (2006) Point based methods for automatic bronchial tree matching and labelling. In: Proceedings of SPIE, Medical Imaging, vol. 6143, March 2006
3. Belongie S, Malik J, Puzicha J (2001) Matching shapes. In: 8th international conference on computer vision, Vol. 1, pp 454–463
4. Bookstein FL (1989) Principal warps: thin-plate splines and the decomposition of deformations. IEEE Trans Pattern Anal Mach Intell 11(6):567–585
5. Urschler M, Bischof H (2005) Assessing breathing motion by shape matching of lung and diaphragm surfaces. In: Proceedings of SPIE Int. Opt. Eng., vol. 5746, pp 440–452, April 2005
6. Coselmon MM, Balter JM, Mc Shan DL, Kessler ML (2004) Mutual information based CT registration of the lung at exhale and inhale breathing states using thin-plate splines. Med Phys 31(11):2942–2948

Coordinated dynamics-based control of robotic couch and MLC-bank for feedforward radiation therapy

Tarun Podder, Ivan Buzurovic, Yan Yu

Department of Radiation Oncology, Kimmel Cancer Center, Thomas Jefferson University Hospital, Philadelphia, PA, USA

Abstract Respiratory and cardiac motions induce displacement and deformation of the tumor-volume in various internal organs. To accommodate this undesired movement and other errors, physicians incorporate a large margin around the tumor to delineate planning target volume (PTV), so that the clinical target volume (CTV) receives the prescribed dose under any scenario. Consequently, a large volume of healthy tissue is irradiated and sometimes it is difficult to spare critical organs adjacent to the tumor. For compensating this tumor motion, three major techniques are used: breath-hold, gating, and active tracking and dynamic delivery (ATDD). Although, ATDD is the most effective technique, it is the most challenging one. The ATDD can be accomplished in three different ways: adjusting the multi-leaf collimator (MLC), adjusting the couch, and adjusting the MLC and couch simultaneously. The first two techniques have been explored and/or implemented in practice. However, the third approach has not been investigated extensively. In our proposed new approach, we decomposed and allocated the tumor motion trajectory to the subsystems (MLC-bank and HexaPOD robotic couch) based on their natural frequency domains using wavelet technique. We deployed a dynamics-based decentralized coordinated closed-loop Proportional, Derivative and Integral (PID) controller to simulate the dynamic behavior of the system. The efficacy of the proposed method has been investigated by extensive computer simulation and the results are presented in this paper.

Keywords Decentralized control · Dynamics-based control · Wavelet decomposition · Robotic radiation therapy · Hexapod robotic couch · Multi-leaf collimator · Dynamic response

1. Introduction

Tumors (i.e., target-volume) in lung, pancreas, liver, prostate, breast, and other organs move significantly during cardiac and breathing cycles. In order to deliver a prescribed dose to the CTV under any conditions, clinicians delineate PTV with a large margin (about 50 mm). Consequently, a large volume of healthy tissue is included in PTV and sometimes it is difficult to spare critical organs adjacent to the tumor. Therefore, it is extremely important to irradiate only the target-volume and minimize the healthy tissue

irradiation by compensating the tumor movement and deformation. Major factors contributing to the overall geometric error and consequently inaccurate/undesired delivery of radiation dose are: (1) inter- and intra observer variations in gross tumor volume (GTV) definition, (2) motion artifacts (respiratory and cardiac) on the computed tomography (CT) images used to define targets and surrounding structures, (3) motion during dose delivery due to respiration and heartbeat, (4) variations caused by changing organ volumes (e.g., bladder filling during setup and treatment), tumor growth or shrinkage, tissue swelling, and (5) patient setup error. Of these factors, respiratory motion is the major contributor to the target movement and deformation in and around the thorax [1]. It is acknowledged that there are significant motion problems for tumors in the lung, breast, esophagus, liver, and kidney. However, due to the lack of appropriate tools, it is common practice to encompass the CTV with a PTV margin that allows for these variations.

Recently, several research groups are investigating various aspects of tumor tracking and developing tools to deliver precise dose to moving target-volume [2–7]. The commonly practiced methods for compensating target/tumor motion are: (1) breath-hold, (2) gating, and (3) active tracking and dynamic delivery (ATDD), however, each of them has its own unique limitations. For example, the MLC gating technique using internal fiducials requires kilovoltage X-ray which delivers unwanted radiation dose to the patient, and additionally gating suffers from severely low duty-cycle (only 30–50%) and intensity modulated radiation therapy (IMRT) efficiency (only 20–50%); all these lead to a 4- to 15-fold increase in delivery time over conventional treatment [1]. Breath-hold technique requires training and is challenging for some patients. Although, ATDD is the most effective technique, it is the most challenging one. The ATDD can be accomplished in three different ways: (1) adjusting the MLC, (2) adjusting the couch, and (3) adjusting the MLC and the couch simultaneously. The first two techniques have been explored and/or implemented in practice. But the third approach has neither been investigated extensively nor been implemented. The commercially available HexaPOD robotic couch is capable of positioning the patient with high accuracy compared to other conventional couches [8], however, currently it does not have provision for compensating the tumor movement due to respiratory and cardiac motion. Recently, a group of researchers has investigated the feasibility of using the treatment couch (HexaPOD and Dynatrac) for intra-fraction motion tracking [7]. Their study concluded that the achievable speed was much less than required to counter respiration-induced tumor motion in the realm of clinically relevant motion amplitudes. Such a robotic system which is subjected to a large load and operating at moderate frequency and amplitude requires not only robust electro-mechanical design but also stable closed-loop dynamic control that can produce a high degree of repeatability and accuracy with varying external perturbations.

In this study, we develop a decentralized closed-loop dynamic controller for adjusting the MLC-bank and robotic couch based on their dynamic response bandwidth so that the target-volume appears to be stationary to the radiation beam and the beam can be delivered close to 100% duty-cycle.

2. Materials and methods

To track the tumor for optimal dose delivery to the CTV with minimal PTV, we propose to control both the MLC-bank and the HexaPOD simultaneously [9, 10]. We have two subsystems (MLC-bank and HexaPOD couch) with vastly different dynamic responses, i.e., natural frequency bandwidths. The trajectory of the tumor movement due to respiratory and cardiac motions is decomposed into two segments (high and low frequency segments) using the Wavelet technique. The high frequency component is assigned to the lighter subsystem, i.e. the MLC-bank, and the low

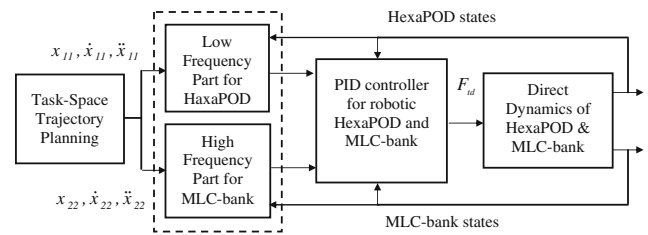


Fig. 1 Block diagram of the decentralized coordinated dynamics-based closed-loop controller for HexaPOD robotic couch and linear accelerator’s MLC-bank

frequency with larger amplitude is allocated to the heavier subsystem, i.e. the couch (Fig. 1).

2.1. System dynamics

We have developed full-fledged dynamic equations of motion for the HexaPOD robotic couch (which is a special type of Stewart Platform, i.e., a parallel robotic manipulator, Fig. 2) and the MLC-banks of the linear accelerator using Lagrangian formulation [11, 12]. Lagrangian function is expressed as: $L = \text{Kinetic energy } K - \text{Potential energy } P$. General form of dynamic equations is:

$$\frac{d}{dt} \left(\frac{\partial L}{\partial \dot{q}} \right) - \frac{\partial L}{\partial q} = \tau \tag{1}$$

We derived the dynamic equations of motion for the whole system in terms of Cartesian coordinates as following form:

$$M(X_{p-o})\ddot{X}_{p-o} + V_m(X_{p-o}, \dot{X}_{p-o})\dot{X}_{p-o} + G(X_{p-o}) = J^T(X_{p-o})F_{td} \tag{2}$$

where, $q \in R^n$ is the vector of generalized joint-space coordinates, $M \in R^{n \times n}$ is the mass (or inertia) matrix, $P(q) \in R^n$ is the potential energy vector, F_{td} (or τ) is the of generalized force vector applied to the system through the legs to drive the platform and $M(X_{p-o}) = M_{up} + M_{Legs}$, $V_m(X_{p-o}, \dot{X}_{p-o}) = V_{m_{up}} + V_{m_{Legs}}$, and $G(X_{p-o}) = G_{up} + G_{Legs}$. The MLC-bank was considered as a lump-mass moving in the horizontal plane.

2.2. Tumor trajectory

Assuming a fixed period for the motion, we have chosen the position of the tumor as a function of time in parametric form as follows [13]:

$$y(t) = y_0 - b \cos^{2n} \left(\frac{\pi t}{\tau} - \phi \right) \tag{3}$$

where y_0 is the position at exhale, b is the extent (amplitude) of the motion, τ is the period of breathing cycle, n is a parameter that determines the general shape (steepness and flatness) of the model,

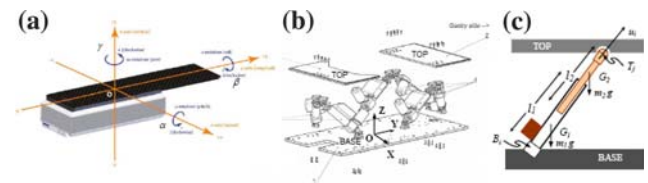


Fig. 2 HexaPOD robotic couch, **a** external isometric view, **b** internal isometric view, and **c** schematic of the leg

and φ is the initial phase of the breathing cycle. For our computer simulation, we have taken $y_0 = 0$, $\tau = 5.7$ s, $b = 1.8$ cm, $n = 1$, and $\varphi = 0$. To make the simulation more realistic, we have incorporated random noise function as

$$y_d(t) = c \text{rand}(1, t) - \frac{c}{2}, \quad c = \text{a constant} \quad (4)$$

Thus, the resultant function of the tumor motion in patient’s superior-inferior direction becomes as follows:

$$s(t) = y(t) + y_d(t) \quad (5)$$

Using wavelet technique (available in MATLAB), we decomposed the Eq. 5 into two segments as $s(t) = a_1(t) + d_1(t)$, where $a_1(t)$ is the low frequency component allocated to the HexaPOD couch and $d_1(t)$ is the high frequency component allocated to MLC-bank, shown in Fig. 3.

3. Results and discussions

The computer simulation results are presented in the Figs. 4 and 5. We observed significant improvement in tumor’s position tracking while the decomposed trajectories were allocated to both the MLC-bank and the HexaPOD couch (Fig. 4, blue line). In contrary, we noticed large residual fluctuating error in tumor tracking when only the HexaPOD couch was used (Fig. 4, green line). The operating forces and torques were presented in Fig. 5, where the largest force is in the vertical direction (shown in red) which mainly balances the weight of the system. Thus, it appears that decentralized dynamics-based controller can track the tumor motion more accurately.

4. Conclusions and future work

The proposed closed-loop dynamics-based control of the robotic couch and MLC-bank was more effective than controlling the couch only to keep track of the moving target-volume. Imple-

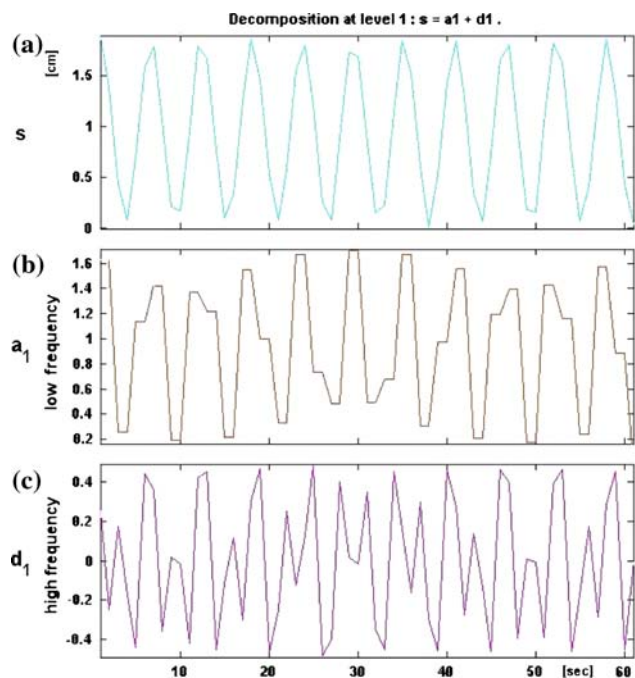


Fig. 3 Wavelet decomposition of the tumor motion, **a** resultant motion, **b** low frequency component, and **c** high frequency component

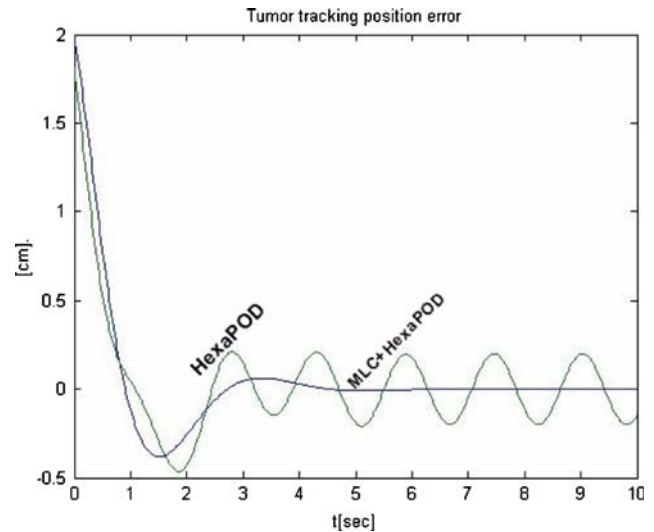


Fig. 4 Tumor tracking errors—using MLC-bank& HexaPOD (blue line) and using HexaPOD only (wavy green line)

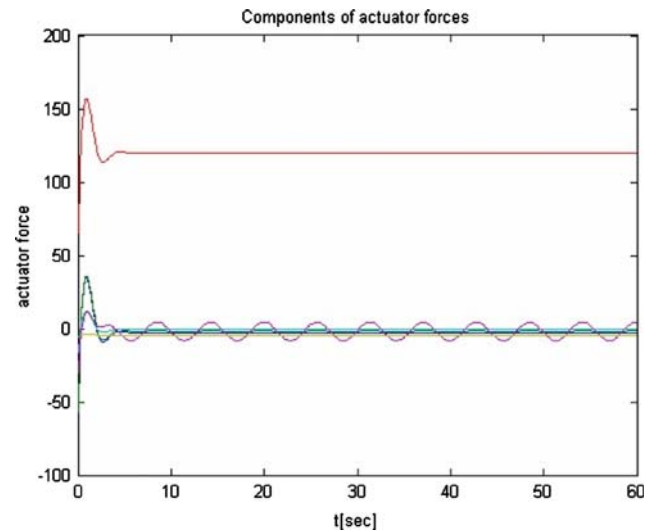


Fig. 5 HexapOD operating forces & torques expressed in task-space

mentation of the proposed technique can potentially improve real-time tracking of the tumor-volume to deliver precise radiation dose at almost 100% duty cycle while minimizing irradiation to health tissues and sparing critical organs. This, in turn, will improve the quality of patient treatment by lowering the toxicity level and increasing survival. In this study, we have deployed a relatively simple closed-loop PID control. Subsequently, we will be investigating the efficacy of the adaptive control and optimal control, if necessary. Adaptive control can be a good choice because of the variability in the payload on the system, i.e., the weight of the patient. One of the main challenges is to synchronize the respiratory motion with the robotic couch and/or IMRT delivery (or 3D conformal radiotherapy) considering the target-volume deformation in addition to target movement. We are working on this aspect of the study.

References

1. Keall PJ, Mageras GS, Balter JM et al (2006) The management of respiratory motion in radiation oncology report of AAPM Task Group 76. *J Med Phys* 33(10):3874–3900
2. Ozhasoglu C, Murphy MJ (2002) Issues in respiratory motion compensation during external-beam radiotherapy. *Int J Radiat Oncol Biol Phys* 52(5):1389–1399
3. Vedam SS, Keall PJ, Docef A, Todor DA, Kini VR, Mohan R (2004) Predicting respiratory motion for four-dimensional radiotherapy. *J Med Phys* 31(8):2274–2283
4. Sharp GC, Jiang SB, Shimizu S, Shirato H (2004) Prediction of respiratory tumour motion for real-time image-guided radiotherapy. *J Phys Med Biol* 49(3):425–440
5. D'Souza W, McAvooy TJ (2006) Analysis of the treatment couch and control system dynamics for respiration-induced motion compensation. *Med Phys* 33(12):4701–4701
6. Keall PJ, Cattell H, Pokhrel D et al (2006) Geometric accuracy of a real-time target tracking system with dynamic multileaf collimator tracking system. *Int J Radiat Oncol Biol Phys* 65(5):1579–1584
7. D'Souza W, Naqvi SA, Yu CX (2005) Real-time intra-fraction motion tracking using the treatment couch: a feasibility study. *Phys Med Biol* 50:4021–4033
8. Chung H, Jin T, Suh T, Palta J, Kim S (2006) Mechanical accuracy of a robotic couch. *J Med Phys* 33(6):2041
9. Podder TK, Sarkar N (2000) Dynamic trajectory planning for autonomous underwater vehicle-manipulator systems. In: *International Conference on Robotics and Automation*, San Francisco, pp 3461–3466
10. Podder TK, Sarkar N (2004) A unified dynamics-based motion planning algorithm for autonomous underwater vehicle-manipulator systems. *J Robotica* 22(1):117–128
11. Craig JJ (1989) *Introduction to Robotics*. Addison-Wesley, New York
12. Lebret G, Liu K, Lewis FL (1993) Dynamic analysis and control of a Stewart platform manipulator. *J Robotic Syst* 10(5):629–655
13. Lujan AE, Larsen EW, Balter JM, Ten-Haken RK (1999) A method for incorporating organ motion due to breathing into 3D dose calculations. *J Med Phys* 26(5):715–720

Sensitivity of parametric deformable image registration to image noise

Martin J Murphy, Zhouping Wei, Mirek Fatyga, Hualiang Zhong
Department of Radiation Oncology, Virginia Commonwealth University, Richmond, USA

Abstract Deformable image registration finds the transformation that maps a source image to a target image. Image quality factors such as noise may influence the accuracy of this mapping. We have analyzed the sensitivity of a B-spline parametric deformable image registration process to noise that is characteristic of cone-beam CT. We find that the registration is insensitive to simulated noise levels that exceed the highest level that would be encountered in routine cone-beam CT studies.

Keywords Deformable image registration · Cone-beam CT

1. Introduction

Image-guided adaptive radiotherapy proposes to use sequential CT studies to track anatomical change during treatment via deformable image registration. These CT studies can be acquired with either conventional fan-beam CT (FBCT) systems or more novel cone-beam CT (CBCT) techniques. In one scenario a fan-beam CT would be used for initial treatment planning, followed by one or more cone-beam CTs for daily anatomy tracking and plan adaptation. However, CBCT images can have higher noise

levels than FBCT at the same level of exposure [1], which might impact image registration accuracy. Furthermore there can be a significant advantage in reducing the patient's daily CBCT radiation dose by decreasing the x-ray exposure in milliamperes-seconds (mAs), which will add more noise to the images. We have investigated the effect of image noise on the deformable registration of fan-beam and simulated cone-beam CTs. Our goal was to see if registration accuracy would be degraded by higher CBCT noise levels.

2. Materials and methods

We have developed a deformable image registration (DIR) process based on parametric B-spline modeling of the anatomical deformation. The general method of B-spline registration is detailed in the literature. The salient feature for this study was the use of an intensity-based sum-of-squared-differences (SSD) for the image similarity metric.

Our noise evaluation study used a sequence of six CT studies for each of ten prostate patients. The first CT for each patient was designated the source CT and the five subsequent CTs were used as target CTs. For each patient the source CT was deformably registered to each target CT to produce a displacement vector field (DVF) describing the flow of anatomy needed to transform the source image into the target image.

Each CT study had the prostate, bladder, and rectum manually contoured by an experienced radiation oncologist. The DVF for each pair of registered images was used to automatically transfer the manual treatment planning contours from the source CT to the target CT.

The accuracy of the automatically transferred contours (and thus of the deformable registration process) was assessed by comparing them to manually-drawn contours on the target images. However, no one set of manual contours can be confidently taken to be exact. I.e., there is no objective gold standard in manual contouring. At best one can establish a clinically plausible range of manual contours and then judge whether the automatic contours fall within that range.

The range of inter-observer variability was estimated in an evaluation test by a second experienced radiation oncologist who had no involvement in the original contouring process. The evaluation was done by having the second physician re-contour the CTs without reference to the initial set of contours. The difference between the two observers' contours was measured as the radial shifting of points on each contour (i.e., the radial difference between the original and the later contours), measured in millimeters at 3-degree intervals around the perimeter of each contour. The same inter-observer test was repeated on another set of prostate images by three different radiation oncologists. The inter-observer differences were collected into frequency histograms. Then, similar radial differences were computed between the manual and automatic target contours. This provided a comparison of the variability between the automatic (deformed) and manual contours in terms of the variability among observers. Figure 1 shows the radial difference histogram for the two-way observer comparison, the three-way observer comparison, and the comparison of automatic to manual contours for the prostate and rectum. Similar comparisons were made for the bladder.

To evaluate DIR noise sensitivity, each target CT was modified to include higher levels of noise characteristic of cone-beam CT and the registration tests were repeated. (The source CTs did not have noise added.) Changes in registration accuracy due to increased noise were detected by monitoring changes in the automatically transferred contours.

The random noise in cone-beam CT images reconstructed via standard methods is not white noise but has a distinctive spatial correlation represented by its power spectrum. These spectra

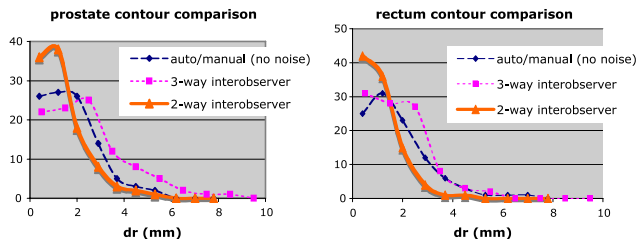


Fig. 1 The distribution of automatic/manual contour variations compared to inter-observer variations for the prostate and rectum, in the absence of added image noise

have been measured by Jaffray and Siewerdsen [1] in images with noise levels corresponding to ± 20 to ± 80 Hounsfield units (HU). We simulated additional CBCT noise in each slice of our target CTs by generating randomized noise images with the same power spectra measured by Jaffray and Siewerdsen [1] and adding them to the original target FBCTs. In our simulation tests we added noise at levels of ± 40 HU (2%), ± 80 HU (4%), and ± 120 HU (6%) to our target FBCT to simulate a wide range of CBCT noise that exceeded what one would expect to observe in a practical CT. Figure 2 shows one slice of a representative source CT alongside the corresponding target slice after modification to include ± 80 HU of additional noise.

We evaluated the effect of noise on the deformable registration accuracy by measuring the changes in the automatic contours as the added noise level in the target images increased from 0 to ± 120 HU. The noisy automatic contours were compared to both the manually-drawn contours on the original target FBCTs and to the automatic contours registered to those original target images in the absence of added noise, using the radial difference methodology described above. The noisy target CBCTs were not manually re-contoured. In this way the comparison excluded the effects of CBCT image quality on manual contouring accuracy, thus providing an objective look at its effects on the automatic process alone.

3. Results

Figure 1 shows that variation of the automatic contours with respect to the manual contours is comparable to the inter-observer variations. Figure 3 compares the automatic contours registered for noisy images to the same contours registered with no added noise. If we compare the automatic contour changes induced by added noise (Fig. 3) to the intrinsic variability of the automatic and manual contours (Fig. 1) we see that the automatic contours of the prostate did not begin to change shape noticeably until an additional 6% (± 120 HU) of noise had been added to the images. Even at that level of noise the change in the rectum contour shapes remained small. This indicates that the registration process itself was largely unaffected by the addition of up to ± 80 HU of CBCT noise and only nominally affected by even higher noise levels. The noisiest CBCT images analyzed by Jaffrey and Siewerdsen [1] corresponded to about ± 80 HU in our simulations. Figure 2 shows that this is a visibly high level of noise that obscures the boundaries of the important organs.

4. Discussion

We found that the additional noise caused no appreciable loss of registration accuracy at magnitudes higher than what would normally be found in an actual cone-beam CT. We conclude that noise levels in cone-beam CT that might be high enough to reduce manual contouring accuracy do not necessarily reduce image

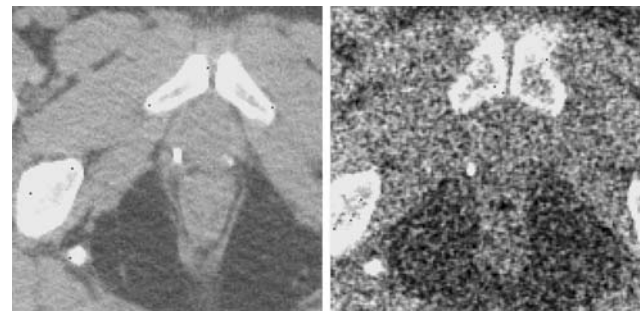


Fig. 2 One slice of the source image compared to the same slice of the simulated CBCT target image with ± 80 HU added noise

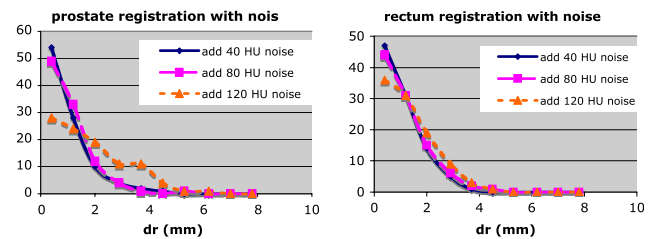


Fig. 3 The changes in the automatic contours as a function of noise in the target image, for added noise levels of up to ± 120 HU. The change is measured relative to the automatic contours registered with no noise

registration and automatic contouring accuracy. This supports the use of cone-beam CT as an imaging modality for image-guided adaptive radiotherapy.

The problem of registering a low-noise source image to a high-noise target image is analogous to matched filter object recognition in a noisy image. In our application the original FBCT image corresponds to the filter template, which is shifted and deformed until it matches a corresponding shape in the noisy target image. Matched filters using the sum-of-least-squares similarity measure are known to provide the optimal signal-to-noise ratio in the presence of white noise [2] and are capable of identifying objects with high confidence at signal-to-noise levels considerably higher than were present in these simulations [3]. However, our simulations involve structured noise, which is a somewhat different situation that might be expected to give less favorable results. Although the present tests suggest that deformable image registration can be accurate and robust in the presence of high levels of CBCT-type structured noise, it is possible that more highly structured noise might begin to bias the registration at spatial resolutions that are comparable to the correlation length of the noise. This question is worth further study.

References

1. Jaffrey DA, Siewerdsen JH (2000) Cone-beam computed tomography with a flat-panel imager: initial performance characterization. *Med Phys* 27(6):1311–1323
2. Van Vleck JH, Middleton D (1946) A theoretical comparison of the visual, aural, and meter reception of pulsed signals in the presence of noise. *J Appl Phys* 17:940
3. Helstrom CW (1960) *Statistical theory of signal detection*. Pergamon, New York

Combined use of tractography and gamma knife radiosurgery three dimensional treatment planning: initial experience

R. I. Foroni¹, G. K. Ricciardi², A. Sboarina¹, C. Lovato¹,
A. De Simone¹, F. Lupidi¹, M. Longhi¹, A. Nicolato¹,
M. Gerosa¹, F. Pizzini², A. Beltramello², H. J. Park³

¹Stereotactic Unit, Neurosurgery Department, University Hospital, Verona, Italy

²Neuroradiology Section, Neurosurgery Department, University Hospital, Verona, Italy

³Laboratory of Molecular Neuroimaging Technology, College of Medicine, Yonsey University, Seoul, Korea

Abstract *Object:* The goal of this study was to assess the feasibility of fusion between diffusion-tensor imaging (DTI), based tractography and pre-radiosurgery stereotactic Magnetic Resonance Imaging (MRI), to evaluate irradiation to eloquent tissue surrounding treated lesions. *Materials and methods:* Eight patients with brain arterio-venous malformation or brain tumor were studied at 3 T to obtain DTI and at 1 T to obtain stereotactic three-dimensional imaging. Fiber tracking of the corticospinal tract (CST) was performed bilaterally in each patient. Finally image registration between 3D corticospinal tractography and 3D T1-weighted stereotactic volumetric study was performed. To verify the accuracy of the registration process the position of the CST at the level of the posterior limb of the internal capsule and of cerebral peduncle was specifically assessed. *Results:* Image registration was feasible in all patients and was performed within 15 min. Location of the CST within the posterior limb of the internal capsule and the cerebral peduncle corresponded to previous reports. *Conclusion:* Integration of tractography, within gamma knife surgery stereotactic imaging planning, is feasible and compatible within a routine clinical setting. Data obtained with this technique may be used to obtain a better estimate of the maximum radiation dose delivered to specific tracts.

Keywords Diffusion-tensor imaging · Gamma knife surgery · Stereotactic radiosurgery · Treatment planning ·

1. Introduction

In the last decade Gamma Knife Stereotactic Radiosurgery has become the 'gold standard' among different therapeutic methods capable of treating solid encephalic lesions through exposure to high radiation doses in a single fraction [1]. Therapeutic success is guaranteed by a very high conformation standard between therapeutic isodose and lesion margins; this strongly reduces undesirable healthy tissue irradiation. However the residual radiation dose affecting eloquent nervous tissue is a potential threat requiring knowledge of the localization of functional anatomic structures surrounding the treated lesion [2]. New imaging techniques such as functional Magnetic Resonance Imaging and diffusion-tensor imaging (DTI) are capable of providing valuable information [3–6] that may be used to reduce irradiation of important functional structures by modifying treatment isodoses [7].

The aim of this study is to evaluate the feasibility of image fusion between DTI and pre-radiosurgery stereotactic imaging to avoid radiation induced damage to motor fibers of the corticospinal tracts (CST) adjacent to cerebral intra-axial lesions treated with Gamma Knife.

2. Materials and methods

2.1. Patients

Eight patients (six males and two females) aged between 20 and 63 were studied. Seven patients were affected with arterio-venous malformations while the eighth had a solitary intra axial metastasis. The anatomical areas involved were: the thalamo-mesencephalic region in six patients and the motor cortex in the remaining

two patients. All lesions were along the presumed course of the CST.

2.2. DTI and fiber tracking

The day before radiosurgery we acquired high resolution T1 weighted isotropic volumetric data set using a 3D-magnetization prepared rapid gradient echo (3D-MPRAGE) sequence with $1 \times 1 \times 1$ mm voxel size. During the same session DTI was performed using a 3T MR unit (Allegra; Siemens, Erlangen, Germany). A diffusion weighted single-shot spin echo, echo planar sequence with $1.7 \times 1.7 \times 3$ mm voxel size (repetition time 7,000 ms, echo time 75 ms, field of view 220 mm, matrix size 128×128 , 3 mm section thickness without intersection gaps, bandwidth ± 1300 Hz.) was employed. Motion-probing gradients were applied along 12 noncolinear directions with a b factor of 700 s/mm^2 after one non-diffusion weighted image ($b = 0 \text{ s/mm}^2$) was obtained. The imaging times for T1 weighted volumetric study and DTI were 11 min.

After appropriate filtering to reduce mismatching due to artifacts from eddy currents, diffusion tensor images were transferred to a Personal computer (Intel P4) and then processed in order to calculate voxel based fractional anisotropy (FA) and to obtain fiber tracks using MatLab based modules developed by one of the authors (DoDTI version 1.2, available at <http://neuroimage.yonsei.ac.kr/dodti/>, HJ Park, Laboratory of Molecular Neuroimaging Technology, College of Medicine, Yonsey University, Seoul, Korea, in cooperation with Martha E. Shenton, Laboratory of Mathematics in Imaging, Dept. of Radiology, Brigham and Women's Hospital, Harvard Medical School, Boston, MA and Carl-Fredrik Westin, Clinical Neuroscience Division, Laboratory of Neuroscience, Boston VA Health Care, System-Brockton Division, Dept. of Psychiatry, Harvard Medical School, Boston, MA).

Tracking of the CST was performed with the continuous tracking method using the two ROI approach. Two ROIs were placed on transverse non-diffusion-weighted images according to established anatomic markers [8]: the first ROI was placed in the precentral gyrus bilaterally and the second ROI in the cerebral peduncle bilaterally.

Propagation in each fiber tract was terminated if a voxel with a FA value of less than 0.15 was reached or if the inner product of two consecutive vectors was greater than 0.75. These conditions prohibited the turning of angles larger than 41° during tracking.

2.3. MRI and radiosurgery

MR imaging was performed under stereotactic conditions on a 1 T unit (Magnetom Harmony Maestro Class, Siemens, Erlangen, Germany) with an MR-compatible Leksell G stereotactic frame (Elekta, Stockholm, Sweden) fixed to the skull under local anesthesia.

The protocol consisted of three sequences: (1) T2 weighted axial fast spin echo (2) post-contrast T1-weighted axial spin echo (3) Magnetic Resonance Angiography was performed by means of post contrast 3D Time of Flight sequence. The total acquisition time was about 15 min.

2.4. Image registration

Registration consisted in matching both high resolution T1-w 3D-MPRAGE and the fiber tracts on the MR study performed under stereotactic conditions by introducing virtual reference points [9, 10]. This process was performed in several steps: (1) initially volumetric spaces of the various MRI datasets were made uniform to allow superimposition of virtual markers in the peripheral portions of non stereotactic images (dilatation process that does not affect the spatial resolution); (2) registration between volumetric study and images acquired under stereotactic conditions: this process was performed by means of rigid body

rototranslation as regards the anterior-posterior commissure at mid sagittal plan. (3) superimposition of stereotactic reference coordinates on corresponding images from the T1-W volumetric data set; in the case of images that could not be overlapped because of different resolution, stereotactic reference coordinates were calculated. (4) After registration with stereotactic coordinates the entire T1-w 3D-MPRAGE dataset with superimposed tracked fibers was then transferred to the computer dedicated for treatment planning (Leksell Gamma Knife Treatment Planning System; Elekta, Stockholm, Sweden); (5) in this way the intersection points of previously selected fibers were visible, marked and coded bright white, in the axial planes. (6) Registration and intersection of tracked fibers on images acquired under stereotactic conditions were performed with software developed with C++ or Tcl/Tk language modules.

To verify the accuracy of the registration process the course of the 3D CST was carefully followed on the images of the volumetric T1-weighted study acquired under stereotactic conditions. The position of the CST at the level of the posterior limb of the internal capsule and of cerebral peduncle was specifically assessed in all cases.

2.5. Evaluation of radiation delivery

The isocontour line of radiosurgical treatment planning was superimposed on the registered images and the exact amount of radiation was noted for the CST of each patient.

3. Results

In seven out of eight patients candidates for radiosurgical treatment it was possible to highlight clearly the fibers of CST (Fig. 1). Regional values of FA evaluated in different locations of image dataset exhibited a trend highly comparable with the data available in literature [11].

The time necessary to perform the whole process of image registration ranged between 10 and 15 min and was compatible with implementation in a routine clinical setting.

After image registration the position of the CST, superimposed on the stereotactic volumetric T1-weighted study, at the level of the posterior limb of the internal capsule was always in its posterior third quarter, as previously reported [8]. Furthermore the CST always passed through the lateral segment of the cerebral peduncle. In the seven cases in which the target of treatment was an AVM, although the location of the lesion was always in proximity to the CST, no significant displacement of fibers was noted. This may be due to the fact that no AVM had significant venous dilatation and that these lesions are usually intermingled within the cerebral parenchyma and do not exert significant mass effect.

However in two cases, although the CST were not involved in the lesion, the presence of small amounts of haemosiderin and of flow related signal void, partially interfered with CST visualization on the side of the lesion. Lateral asymmetry between the number of right and left hemisphere fibers was in fact higher than previously reported [12].

Superimposition of extracted fibers on the study acquired under stereotactic conditions to perform treatment planning improved calculation of the exact amount of radiations involving CST.

4. Discussion

DTI is a relatively new imaging modality which enables the anatomical neuronal connectivity of white matter to be observed [5]. In this research our goal was to evaluate clinical feasibility to fuse diffusion tensor tractography of the CST on the stereotactic treatment plan in order to predict the presence of hot spots of radiosurgery dose delivery incorporating relevant motor fiber bundles.

Although several steps were necessary to perform the registration process, this was always carried out within 15 min, without significant delay of treatment planning. Furthermore reliability of the process proved to be good as in all cases the 3 days tracked

CST was superimposed on the established anatomic points where this track is known to be found [8].

An important advantage of our strategy is that it allows inclusion in the stereotactic treatment planning not only of fiber tractography but also of the 3 T non-stereotactic imaging dataset that cannot be acquired with the Leksell G stereotactic frame because of the serious imaging distortion artifacts that would occur.

It has recently been reported that depiction of most fiber tracts is improved at 3 T DT fiber tractography compared with depiction at 1.5 T tractography [13].

Because of its non invasiveness and short time of acquisition and post-processing this technique could easily be introduced in standard stereotactic radiosurgical treatment planning, or more widely in all cases of stereotactic guidance of minimally invasive neurosurgery beyond academic interest of neuroanatomy.

Stereotactic radiosurgery treatment of intracranial lesions enables non-invasive procedures without skull opening; in such conditions intra-procedural tissue shift, which is a major problem in conventional neurosurgery, will not affect overlapping of functional imaging on stereotactic images for treatment planning [14].

In this study in two cases lateral asymmetry between the number of right and left hemisphere fibers was higher than previously reported [12]. This may be due to the fact that diffusion weighted single-shot echo planar sequences are very sensitive to magnetic field perturbations caused by ferromagnetic deposits and flow. Consequently FA anisotropy maps are sometimes partially degraded. A solution to this problem could be to modify the sequence in order to reduce echo time and slice thickness and thus sensitivity to magnetic susceptibility [15].

To our knowledge, only one other group has already reported a similar experience [16] but in their study DTI was performed with a 1.5 T MR imaging unit and most of the stereotactic imaging study were performed with CT.

The present study demonstrates that integration of tractography, within gamma knife surgery stereotactic planning, is feasible and compatible within a routine clinical setting.

Data obtained with this technique may be used to obtain a better estimate of the maximum to specific tracts. This could be useful both to analyze the relationship between the volumes of tracts receiving high radiation doses and subsequent development of a complication, and to modify treatment planning according to complication rates.

References

- Luxton G, Petrovich Z, Jozsef G, Nedzi La, Apuzzo MI (1993) Stereotactic radiosurgery: principles and comparison of treatment methods. *Neurosurgery* 32:241–259; discussion 259
- Sasaki T, Kurita H, Saito I et al (1998) Arteriovenous malformations in the basal ganglia and thalamus: management and results in 101 cases. *J Neurosurg* 88:285–292
- Basser PJ, Jones DK (2002) Diffusion-tensor MRI: theory, experimental design and data analysis—a technical review. *NMR Biomed* 15:456–467
- Hasan KM, Basser PJ, Parker DI, Alexander AI (2001) Analytical computation of the eigenvalues and eigenvectors in DT-MRI. *J Magn Reson* 152:41–47
- Masutani Y, Aoki S, Abe O, Hayashi N, Otomo K (2003) MR diffusion tensor imaging: recent advance and new techniques for diffusion tensor visualization. *Eur J Radiol* 46:53–66
- Pajevic S, Aldroubi A, Basser PJ (2002) A continuous tensor field approximation of discrete DT-MRI data for extracting microstructural and architectural features of tissue. *J Magn Reson* 154:85–100
- Leber KA, Bergloff J, Pendl G (1998) Dose-response tolerance of the visual pathways and cranial nerves of the cav-

- ernous sinus to stereotactic radiosurgery. *J Neurosurg* 88:43–50
8. Holodny AI, Gor DM, Watts R, Gutin PH, Ulug AM (2005) Diffusion-tensor MR tractography of somatotopic organization of corticospinal tracts in the internal capsule: initial anatomic results in contradistinction to prior reports. *Radiology* 234:649–653. Epub 2005 Jan 2021
 9. Ardekani BA, Braun M, Hutton BF, Kanno I, Iida H (1995) A fully automatic multimodality image registration algorithm. *J Comput Assist Tomogr* 19:615–623
 10. Ng L, Ibanez L (2004) Medical image registration: concepts and implementation. In: Peters AK (ed) *Insight into images*. Wellesley, Massachusetts, pp 239–306
 11. Reich DS, Smith SA, Jones CK et al (2006) Quantitative characterization of the corticospinal tract at 3 T. *AJNR Am J Neuroradiol* 27:2168–2178
 12. Lazar M, Field AS, Lee J et al (2004) Lateral asymmetry of superior longitudinal fasciculus: a white matter tractography study (abstr). In: *Proceedings of the 12th meeting of the international society of magnetic resonance in medicine*. International Society of Magnetic Resonance in Medicine, Berkeley, pp 1290
 13. Okada T, Miki Y, Fushimi Y et al (2006) Diffusion-tensor fiber tractography: intraindividual comparison of 3.0-T and 1.5-T MR imaging. *Radiology* 238:668–678. Epub 2006 Jan 2005
 14. Levivier M, Massager N, Wikler D et al (2004) Use of stereotactic PET images in dosimetry planning of radiosurgery for brain tumors: clinical experience and proposed classification. *J Nucl Med* 45:1146–1154
 15. Naganawa S, Koshikawa T, Kawai H et al (2004) Optimization of diffusion-tensor MR imaging data acquisition parameters for brain fiber tracking using parallel imaging at 3 T. *Eur Radiol* 14:234–238
 16. Maruyama K, Kamada K, Shin M et al (2005) Integration of three-dimensional corticospinal tractography into treatment planning for gamma knife surgery. *J Neurosurg* 102:673–677

Prediction of respiratory motion with a multi-frequency based Extended Kalman Filter

L. Ramrath^a, A. Schlaefler^a, F. Ernst^a, S. Dieterich^{2b}, A. Schweikard^a

^aInstitute for Robotics and Cognitive Systems, University of Luebeck, Luebeck, Germany

^bSonja Dieterich, Department of Radiation Medicine, Georgetown University Hospital, Washington, USA

Abstract In this work, an Extended Kalman Filter formulation for respiration motion tracking is introduced. Based on the assumption of multiple sinusoidal components contributing to respiratory motion, a state-space model is developed. Performance of the filter is tested on data sets of patients subject to radiotherapy. Comparison to an nLMS predictor shows that the Kalman filter is less sensitive to systematic errors during target prediction.

Keywords Respiration motion compensation · Extended Kalman filter · Prediction

1. Introduction

Recent technological developments have enabled highly precise image guided radiosurgical treatment to targets outside the skull. Using high resolution stereoscopic X-ray imaging the tumour region can be localized either directly or by means of artificial landmarks, e.g. implanted gold fiducials [1]. However, tumours in the thorax and abdomen are often subject to movements,

primarily due to respiratory motion. New systems to move the treatment beams accordingly have been proposed [1, 2] and currently the robotic CyberKnife is used for motion compensated treatment in clinical practice at numerous sites.

Although respiratory motion is cyclic, the motion pattern varies over time. Hence it is necessary to constantly monitor the motion and to generate control sequences to move the beam synchronously. The signal processing step and the mechanical inertia of the robotic system cause a small but noticeable system delay. In order to precisely compensate for target motion it is thus important to predict its position.

Different approaches to respiratory motion prediction exist. Two major types can be distinguished: model-based and non-model-based predictors. Approaches not based on an explicit motion model include linear prediction, normalized Least-Mean-Squares (nLMS) prediction, and prediction with artificial neural networks [3, 4]. Model-based predictors incorporate certain assumptions on the dynamics of the respiratory motion in order to improve the prediction. For organ motion, models based on trigonometric functions can be used. A more general model-based prediction method is provided by the framework of the Kalman filter providing prediction capability based on the system dynamic behaviour. Existing approaches to Kalman filter prediction do not incorporate an exact model of the respiratory motion. This work therefore presents a Kalman filter based on an augmented sinusoidal motion model incorporating multiple frequencies. As the assumed model is nonlinear, the Extended Kalman filter formulation is applied. The predictor has been tested on a set of motion data from actual patients, and its performance is compared to that of an nLMS predictor with optimal parameter settings. Experimental results indicate that the EK filter is a reliable alternative for respiratory motion prediction.

2. Methods

In order to apply a Kalman filter based predictor, a suitable model for the respiratory motion needs to be developed. In [4], a Kalman filter for respiratory motion prediction is introduced. The proposed filter is based on a linear state space model with an unknown number of states. However, respiratory motion is typically non-linear and has been found to correlate well with a sinusoidal model [5]. Yet, mean position, amplitude and period length show significant cycle-to-cycle variations. This motivates using the Extended Kalman (EK) filter which is applicable to problems with nonlinear models, e.g. to frequency tracking in case of slowly time-varying frequencies [6]. Simple sinusoidal models have been proposed for covering respiratory motion patterns (e.g. [7]). Frequency domain analysis of respiratory motion shows, however, that more than one frequency contributes to the respiratory motion. This motivates the introduction of a multi-frequency state space-model within the EK filter framework to respiratory motion prediction. The model is therefore extended to a sum of n simple sinusoidal models:

$$y(t) = z_0(t) + A_1(t) \sin(\omega_1(t)t + f_1) + A_1(t) \sin(\omega_1(t)t + f_2) + \dots + A_n(t) \sin(\omega_n(t)t + f_n)$$

The discrete EK filter is based on two principal equations, the system equation and the output equation. The first equation relates the states to the input and previous states and the latter equation establishes the predicted output of the system with respect to the system states and the input. For a single frequency, three states are introduced:

the amplitude, the frequency and the phase. Prediction is performed by evaluating the output equation at time step $k + \eta Ts$, where k is the current time step and ηTs is the expected system delay in terms of the sampling rate T_s . Note that for motion prediction only the output equation contains the nonlinear terms, while the system equation is completely linear.

The EK filter is compared to an nLMS predictor, which is often used in textbooks as a simple and robust predictor. In the field of respiratory motion prediction, the nLMS presents a simple approach to predict motion patterns with a linear model [8]. There are essentially two parameters: the number of learning steps M and the learning gain μ (see e.g. [8]).

Prediction performance is evaluated by the following measures:

1. root-mean-square error between predicted and measured signal,
2. maximum error between predicted and measured signal,
3. spectrum power of the error signal at the major respiration frequency.

The tests were performed on data sets from four different patients subject to radiotherapy of the pancreas. Each patient underwent three consecutive sessions of treatment. Respiratory motion of the chest was measured by an infrared tracking system at approximately 26 Hz. For nLMS, an optimal learning factor μ was obtained by analyzing the first 2000 points of data (approximately 75 s) in each set separately. The number of initial values of the frequencies for the EK filter was based on a frequency analysis of the same training data set.

3. Results

Table 1 summarizes the results for four different patients and two (patient 26) or three (the other patients) treatment fractions per patient. In this case the number of frequencies was chosen to be $n = 13$. The programme was allowed to automatically pick the ten frequencies with the highest energy on the first 2,000 sampling points. Then a very low frequency (0.000001 Hz) was added to model the constant trend and the frequency of highest energy was bracketed by one a little lower and one a little higher to emphasize the importance of this frequency. Initial amplitudes were chosen according to the frequencies' power ratios. Prediction was made for the respiration state in $\eta Ts = 200$ ms which, in our setup, corresponds to approximately five time steps.

It can be seen that the EK and nLMS lead to a comparable mean error, the EK being a little better. The maximum error for the Extended Kalman filter, however, is often substantially lower than the maximal error for the nLMS. When looking at the 90% confidence interval (i.e. 90% of the errors are smaller

than this value), we see that the nLMS and the EK usually perform similarly, the EK being a little better in most cases. A frequency analysis shows that the error signal of the nLMS provides higher energy at the main frequency of the respiration, see Fig. 1. This indicates that the nLMS error, although small on average, is substantial at certain stages in the breathing, compare also Fig. 2. The points labelled (a) and (b) in Fig. 2 mark positions in the signal where the nLMS prediction is significantly worse than the EK. As mentioned before, these points usually occur towards the end of the inhalation and exhalation phases. This behaviour comes from the linearity of the nLMS prediction process which tends to react too late to changes in signal curvature. It can clearly be seen that the distance between two points labelled (a) is approximately three

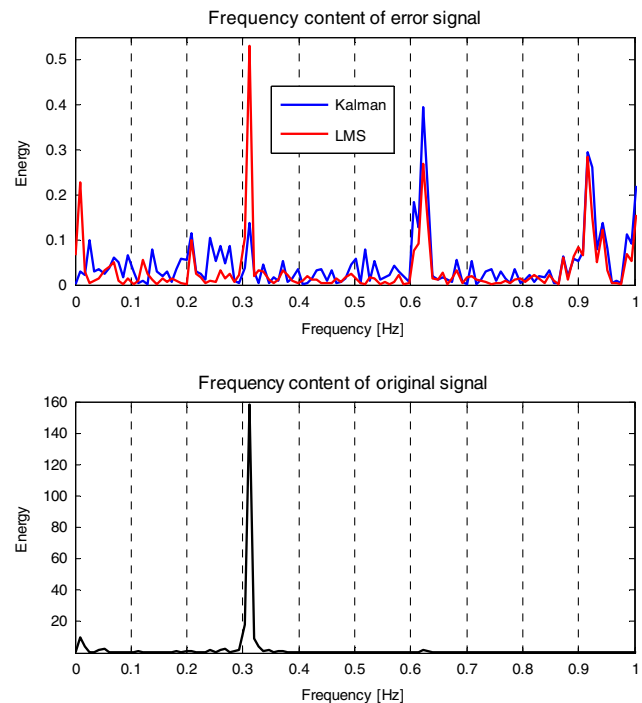


Fig. 1 Frequency content of one data set (db45PANMarker3_frac89_x)

Table 1 Results showing the signal name, the nLMS and EK RMS error, 90% confidence interval, the maximum error and the ratio of the spectrum power nLMS/EK at the frequency with the highest energy in the original signal

Signal	RMS		90% CI		Max. error		Power ratio
	nLMS	EK	nLMS	EK	nLMS	EK	
db17PANMarker1_frac89_x	0.0694	0.0680	0.1156	0.1118	0.2328	0.2415	0.0313
db17PANMarker1_frac90_x	0.1783	0.1527	0.2709	0.2487	0.8421	0.5829	0.1890
db17PANMarker1_frac91_x	0.2084	0.1881	0.2771	0.3069	1.7149	0.9232	5.1705
db26PANMarker1_frac89_x	0.0926	0.0737	0.1563	0.1226	0.3415	0.2473	0.0939
db26PANMarker1_frac90_x	0.1766	0.1747	0.2899	0.2872	0.6667	1.0677	0.2005
db45PANMarker3_frac89_x	0.0993	0.0873	0.1615	0.1417	0.4749	0.3836	0.2582
db45PANMarker1_frac90_x	0.1318	0.1160	0.1865	0.1829	1.6220	0.9459	0.3454
db45PANMarker2_frac91_x	0.0906	0.0875	0.1507	0.1446	0.3912	0.3712	2.2288
db46PANMarker2_frac89_x	0.1760	0.1641	0.2612	0.2701	1.2147	0.7233	0.0994
db46PANMarker3_frac90_x	0.1391	0.1250	0.2127	0.2019	0.8243	0.5092	1.3061
db46PANMarker3_frac91_x	0.1370	0.1152	0.2202	0.1886	0.5891	0.4093	2.1423

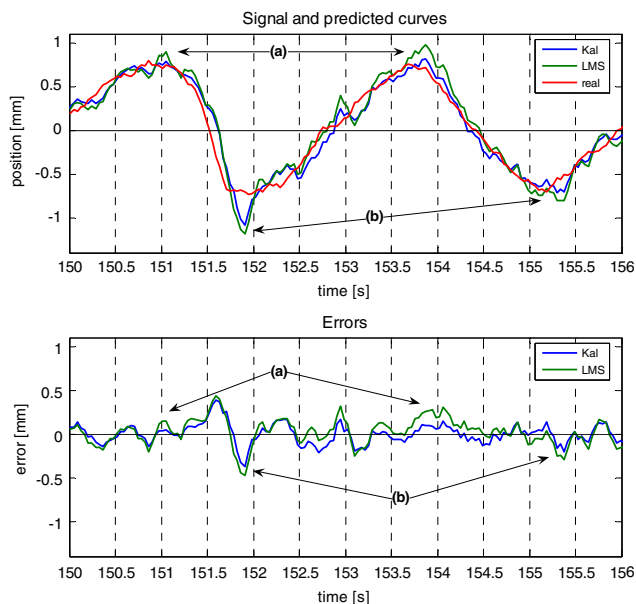


Fig. 2 Prediction errors of one data set (db45PANMarker3_frac89_x)

seconds (as is the distance between two points labelled (b)). This explains why the error signal of the EK prediction has a lower energy at the dominating frequency.

In certain cases (e.g. db17PANMarker1_frac91_x) the ratio becomes larger than one: a possible explanation is that the signals in question had relatively low amplitude, were rather irregular or featured long breathing pauses between exhalation and inhalation. These three cases are all tough to handle for the EK algorithm: low amplitude comes with relatively high noise; irregularity or long pauses characterize a signal which is hard to model by a sinusoidal model. Another important remark on the accuracy of the EK must be made: under certain circumstances, a small shift of the input signal (by one to five sampling points) resulted in a significant increase of the prediction error of the EK predictor. Since this behaviour could not be observed for the nLMS predictor, it can probably be attributed to the linearization process of the Kalman filtering.

4. Conclusions

The Extended Kalman filter is a viable alternative for the prediction of respiratory motion. While the average prediction error is comparable to that of Least-Mean-Squares prediction, the latter is unevenly distributed over the breathing cycle. This implies that a systematic error is introduced when predicting certain target positions, which could add up to affect the dose distribution. The Extended Kalman filter is less prone to such errors and a good candidate for prediction in motion compensated image guided radiation therapy.

References

1. Schweikard A, Glosser G, Bodduluri M, Murphy MJ, Adler JR (2000) Robotic motion compensation for respiratory movement during radiosurgery. *Comput Aid Surg* 5:263–277
2. Keall PJ, Kini VR, Vedam SS, Mohan R (2001) Motion adaptive x-ray therapy: a feasibility study. *Phys Med Biol* 46:1–10
3. Murphy MJ, Dieterich S (2006) Comparative performance of linear and nonlinear neural networks to predict irregular breathing. *Phys Med Biol* 51:5903–5914

4. Sharp G, Jiang S, Shimizu S, Shirato H (2004) Prediction of respiratory tumour motion for real-time image guided radiotherapy. *Phys Med Biol* 49:425–440
5. George R, Vedam S, Chung T, Ramakrishnan V, Keall P (2005) The application of the sinusoidal model to lung cancer patient respiratory motion. *Med Phys* 32:2850–2861
6. Scala BL, Bitmead R (1996) Design of an extended kalman filter frequency tracker. *IEEE Trans Signal Process* 44:739–742
7. Lujan A, Larsen EW, Balter J, Haken RT (1999) A method for incorporating organ motion due to breathing into 3D dose calculations. *Med Phys* 26:715–720
8. Haykin S (2002) Adaptive filter theory, 4th edn. Prentice Hall, Englewood Cliffs

Objective specific beam generation for image guided robotic radiosurgery

A. Schlaefler^a, O. Jungmann^a, W. Kilby^b, A. Schweikard^a

^aInstitute for Robotics and Cognitive Systems, University of Lübeck (D), Luebeck, Germany

^bAccuray Inc., Sunnyvale, CA, USA

Abstract Robotic radiosurgery enables precise dose delivery throughout the body. Planning for robotic radiosurgery comprises of finding a suitable set of beams and beam weights. The problem can be addressed by generating a large set of candidate beams, and selection of beams with nonzero weight by mathematical programming. We propose to use different randomized beam generation methods depending on the type of lesion and the clinical objective. Results for three patient cases indicate that this can improve the plan quality.

Keywords Radiosurgery · Inverse planning · Beam orientation optimization

1. Introduction

Robotic radiosurgery systems are becoming increasingly versatile. Initially the robotic CyberKnife system was developed as means for radiosurgery. Using the robot mounted linac to deliver dose from many directions it is possible to precisely shape a highly target conformal dose distribution with steep gradients towards surrounding tissue.

However, given advances in image guidance and navigation, such systems are no longer limited to typical radiosurgical targets, e.g., brain lesions. Instead, lesions in thorax and abdomen are also treated, including tumors in the prostate, lung, or near the spine. For mobile targets the robotic arm enables respiratory motion compensation, a unique feature of this technology [1].

While one of the advantages of the robotic beam delivery remains the superior conformality, other treatment planning objectives become important for extracranial targets. The high degree of conformality is related to the large number of potential beams, which start at one of approximately 100 different positions covering a large solid angle around the patient and are directed to arbitrary points inside the target. Selecting suitable beams from this large number of possibilities is thus one of the challenges in treatment planning for robotic radiosurgery.

We study whether a beam generation specific to the prime treatment planning objective can improve the treatment plans. Three different placement strategies are compared on actual patient data for three different clinical objectives.

2. Methods

Different approaches to generate candidate beams for radiation therapy exist, including a variety of exhaustive and stochastic search methods [2–4]. For robotic radiosurgery, an approach based on randomized generation of candidate beams and subsequent beam weighting by linear programming has been

proposed [5, 6]. We have implemented this beam generation method, which works as follows:

1. A set M of uniformly distributed points on the target surface is generated.
2. One of the beam source positions is selected as start point S .
3. A point T from M is randomly determined, using a uniform probability distribution.
4. If the beam defined by ST is not part of the candidate beam set C , add it to C .
5. Solve the linear program to assign beam weights
6. Remove all beams with zero weight

The steps 2–4 are repeated until a sufficiently large set of candidate beams has been generated.

We refer to this method as random-surface-beam algorithm (RSB). We have also implemented two alternative methods which differ in the first step. The random-volume-beam algorithm (RVB) computes M as a set of points uniformly distributed over the 3D target volume. The random-projection-beam algorithm (RPB) computes a set of points uniformly distributed on a projection of the target onto a plane perpendicular to the line defined by beam source point and target centroid.

The three methods were applied to three different types of clinical cases with the following clinical objectives: (a) treatment time reduction, (b) improved target coverage by the prescription dose, and (c) more homogeneous dose distribution. Type A typically includes lung tumors, where conformality and homogeneity of the treatment achieved with robotic beam delivery are usually clinically acceptable, but a reduction in total beam weight (measured in monitor units) can shorten the treatment time. An example for type B targets are lesions in close proximity of the spinal cord, for which it is the prime objective to cover most of the lesion with the prescribed dose while avoiding an overdose to the spinal cord. Type C typically includes prostate tumors, for which a homogeneous dose distribution is sought. The measure for homogeneity is the homogeneity index (HI), with an ideal value of unity.

The effect of the candidate beam set size on the planning objective was evaluated by increasing $|C|$ ten times, and solving the same optimization problem repeatedly. Each time 12 beams per beam source position were added, such that the beams were uniformly distributed over the set of beam source positions. The beam weight optimization was performed by solving the linear program using the Cplex solver (Ilog, France).

3. Results

Experimental results for a lung, a spine, and a prostate case are summarized in Figs. 1, 1, and 1. As the beam placement is based on a random selection, each experiment was repeated ten times. For each experiment the results are plotted together with a smoothed trend line.

As can be seen from the figures, the quality metrics improve as subsequently more beams are added, while the standard deviation decreases. This indicates that the solution moves closer towards a globally optimal value. If all potential beams had been placed, linear programming would yield a global optimum.

However, the different beam placement strategies exhibit a different behavior for different clinical objectives. Figure 1 indicates that on average a lower number of total monitor units results from generating beams with the RVB algorithm, compared to the other two algorithms. For optimizing the coverage, the RSB algorithm typically leads to superior results for each iteration, see Fig. 2. If the HI is the metric to be optimized, the best results can be expected when using the RPB algorithm, as shown in Fig. 3. It yields a beam weighting with excellent homogeneity with less than 2,000 candidate beams, while RSB and RVB need up to twice that number of candidate beams to yield a similar solution.

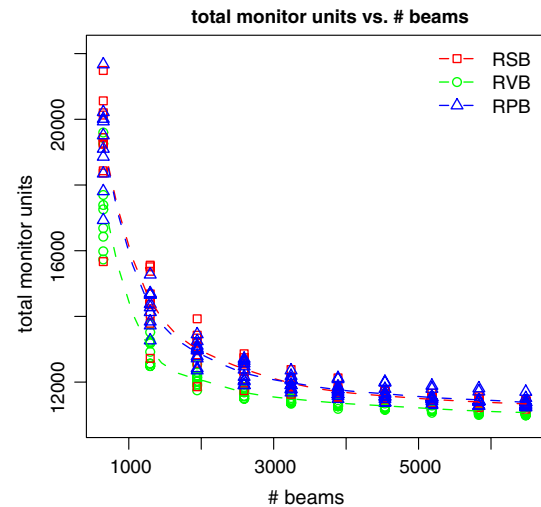


Fig. 1 Results for the lung case. The primary objective is to decrease the total monitor units and improves with the increased number of candidate beams

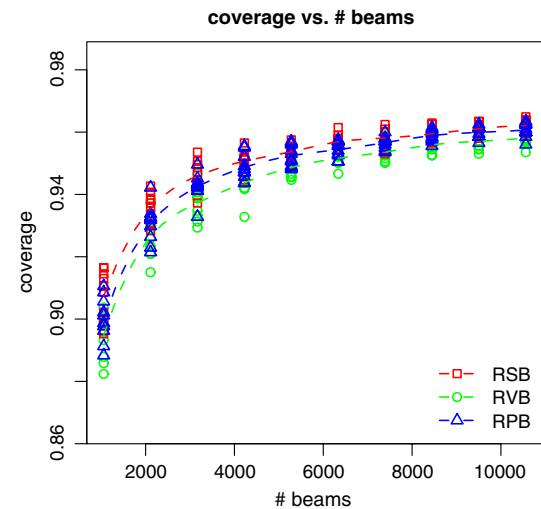


Fig. 2 Results for the spine case. The primary objective is to increase the coverage and improves with the increased number of candidate beams

It is worth noting that the other plan quality metrics did not degrade in a clinically relevant way and are often also improved with a growing number of candidate beams.

4. Conclusion

If we could consider all potential treatment beams, a linear programming based optimization of the treatment planning problem would always yield a global optimum. Of course, even with a rather coarse discretization we cannot hope to solve such a problem for robotic beam placement in a timely manner. Hence heuristics to generate a good candidate set of potential treatment beams are important for practical planning.

Heuristics based on a randomized selection of candidate beams have been shown to be robust and practical. We have investigated, whether this concept can be extended to an objective specific beam generation. Our results indicate that this is

possible, and that improvements in the plan quality can be expected.

References

1. Schweikard A, Glosser G, Bodduluri M, Murphy MJ, Adler JR (2000) Robotic motion compensation for respiratory movement during radiosurgery. *Comput Aided Surg* 5(4):263–277
2. Rowbottom CG, Webb S, Oldham M (1999) Beam orientation customization using an artificial neural network. *Phys Med Biol* 44:2251–2262
3. Wang X, Zhang X, Dong L, Liu H, Wu Q, Mohan R (2004) Development of methods for beam angle optimization for IMRT using an accelerated exhaustive search strategy. *Int J Radiat Oncol Biol Phys* 60(4):1325–1337
4. Hou Q, Wang J, Chen Y, Galvin JM (2003) Beam orientation optimization for IMRT by a hybrid method of the genetic algorithm and the simulated dynamics. *Med Phys* 30(9):2360–2367
5. Schweikard A, Bodduluri M, Adler JR (1998) Planning for camera-guided robotic radiosurgery. *IEEE Trans Robotics Autom* 14(6):951–962
6. Schweikard A, Schlaefler A, Adler JR (2006) Resampling: an optimization method for inverse planning in robotic radiosurgery. *Med Phys* 33(11):4005